Elastic least-squares reverse-time migration using the energy norm

Daniel Rocha & Paul Sava
Center for Wave Phenomena, Colorado School of Mines

ABSTRACT

Incorporating anisotropy and elasticity into least-squares migration (LSM) is an important step towards more accurate amplitudes in seismic imaging. In this context, we derive linearized modeling and migration operators based on the energy norm for elastic wavefields in arbitrary anisotropic media. We use these operators to perform anisotropic least-squares reverse time migration (LSRTM) and generate scalar images that represent subsurface reflectivity and correctly predict observed data without costly decomposition of wave modes. Imaging operators based on the energy norm have no polarity reversal at normal incidence and remove backscattering artifacts caused by sharp interfaces in the Earth model, thus accelerating convergence and generating images of higher quality when compared to images produced by conventional methods. With synthetic and field data experiments, we show that our elastic LSRTM method generates high-quality images that predict the data at receivers locations for arbitrary anisotropy, without the complexity of wave-mode decomposition and with high convergence rate.

Key words: anisotropy, least-squares migration, multicomponent, elastic, reverse time migration

1 INTRODUCTION

The search for more reliable seismic images and additional subsurface information, such as fracture distribution, drives advances in seismic acquisition, such as larger offsets, wider azimuths and multicomponent recording. All of these advances facilitate incorporating anisotropy and elasticity into wavefield extrapolation and reverse time migration (RTM), which is the state-of-art wavefield imaging algorithm suitable for complex geological structures (Baysal et al., 1983; McMechan, 1983; Lailly, 1983; Levin, 1984; Chang and McMechan, 1987; Hokstad et al., 1998; Zhang and Sun, 2009; Farmer et al., 2009). Although seismic acquisition improves with such advances, it always involves practical limitations, such as finite and irregular data sampling, that negatively impact anisotropic elastic wavefield migration. Consequently, this type of migration often leads to images with poor resolution and unbalanced illumination due to such practical acquisition constraints, even though image amplitudes are more reliable compared to acoustic and/or isotropic imaging (Lu et al., 2009; Phadke and Dhubia, 2012; Hobro et al., 2014; Du et al., 2014).

A common solution to these limitations is the implementation of least-squares reverse time migration (LSRTM), which iteratively attenuates artifacts caused by truncated acquisition and provides high-quality images that best predict observed data at receiver locations in a least-squares sense (Chavent and Plessix, 1999; Nemeth et al., 1999; Kuhl and Sacchi, 2003; Aoki and Schuster, 2009; Yao and Jakubowicz, 2012; Dong et al., 2012). However, to overcome these issues from acquisition and to exploit the advantages of more realistic wave extrapolation, some authors propose LSRTM that accounts for multiparameter Earth models, which can either incorporate solely anisotropy (Huang et al., 2016), elastic (Duan et al., 2016; Feng and Schuster, 2016; Xu et al., 2016; Alves and Biondi, 2016; Ren et al., 2017), or viscosity effects (Dutta and Schuster, 2014; Sun et al., 2015). For instance, the visco-acoustic and pseudo-acoustic implementations define Earth reflectivity in terms of contrast from a single model parameter (Dutta and Schuster, 2014; Huang et al., 2016) or in terms of a scalar image based on conventional cross-correlation between wavefields (Sun et al., 2015). Alternatively, elastic LSRTM implementations in isotropic media provide multiple images that are defined in terms of cross-correlation between decomposed wave modes (Duan et al., 2016; Feng and Schuster, 2016; Xu et al., 2016; Alves and Biondi, 2016). However, wave-mode decomposition in anisotropic media is costly and not as straightforward as in isotropic media; and therefore,

anisotropic wave-mode decomposition remains a subject of ongoing research (Yan and Sava, 2009; Zhang and McMechan, 2010; Yan and Sava, 2011; Cheng and Fomel, 2014; Sripanich et al., 2015; Wang et al., 2016).

Incorporating both elasticity and anisotropy into LSRTM is possible with elastic wavefield imaging using the energy norm (Rocha et al., 2017). This type of imaging exploits realistic vector displacement field extrapolation within a multiparameter anisotropic and elastic Earth model, and generates scalar images of the subsurface without costly decomposition of wave modes. As opposed to more conventional imaging conditions, the elastic imaging condition based on the energy norm exhibits no polarity reversal at normal incidence, and computes an appropriate correlation between wavefields that attenuates low-wavenumber artifacts caused by waves that do not correctly characterize subsurface reflectivity (e.g. wave backscattering from salt interfaces). Such artifacts are harmful to the LSRTM inversion and retard convergence because they do not accurately characterize reflections in the subsurface. One outstanding issue with energy imaging is the physical interpretation of the scalar image; we interpret the resulting amplitudes as a measure of energy transfer between incident and reflected wavefields, in contrast with more conventional images that represent amplitude conversion for different incident and reflected wave modes. As for any other wavefield migration method, its quality suffers from the acquisition limitations discussed earlier. Therefore, we define a linearized modeling operator that generates anisotropic elastic scattered wavefields, and we propose a LSRTM method that uses the energy image as a proxy for the reflectivity model. This LSRTM method is ideal to generate high-resolution images that correctly predict observed multicomponent data, without the shortcomings of different wave modes and full-wavefield phenomena present in anisotropic elastic wavefields. We demonstrate all the benefits of the method with synthetic and field data experiments.

2 THEORY

We can express elastic wavefield migration with mathematical operators such that

$$\mathbf{m} = \mathbf{L}^{\mathrm{T}}\mathbf{d}_r \ , \tag{1}$$

where $\mathbf{L}^{\mathrm{T}}$ is the migration operator, $\mathbf{d}_r$ is single-scattered multicomponent data recorded at receiver locations, and $\mathbf{m}$ is an image or a set of images associated with the Earth reflectivity. The operator $\mathbf{L}^{\mathrm{T}}$ involves backpropagation of $\mathbf{d}_r$ through an Earth model generating a receiver wavefield $\mathbf{U}_r$, and the application of an imaging condition comparing $\mathbf{U}_r$ with the source wavefield $\mathbf{U}_s$ (extrapolated from a source function and location). For instance, an elastic imaging condition can involve decomposition of the wavefields $\mathbf{U}_s$ and $\mathbf{U}_r$ into separated wave modes and the application of crosscorrelation between wave modes (Yan and Sava, 2007). One generally considers wavefield migration as the adjoint operator of linearized modeling (also known as single-scattering modeling) (Claerbout, 1992). Therefore, $\mathbf{L}$ is the linearized modeling operator such that

$$\mathbf{d}_r = \mathbf{L}\mathbf{m} \ , \tag{2}$$

and generates single-scattering data $\mathbf{d}_r$ at receiver locations using an image containing reflectors that act as sources under the action of the background (or source) wavefield $\mathbf{U}_s$ (embedded in the operator $\mathbf{L}$).

Therefore, we define $\mathbf{m}$ as reflectivity that depends on a particular imaging condition and is not necessarily defined in terms of contrasts in the Earth model. The same principle applies to the linearized modeling operator $\mathbf{L}$, which we define as an adjoint operator of a migration operator that utilizes a certain imaging condition, and $\mathbf{L}$ is not necessarily related to the physics of single scattering.

2.1 Energy-norm linearized modeling and migration operators

For two anisotropic elastic source and receiver wavefields, which are functions of space $\mathbf{x}$ and time t $\mathbf{U}_s(\mathbf{x},t)$ and $\mathbf{U}_r(\mathbf{x},t)$, we can form an image using the energy imaging condition (Rocha et al., 2017):

$$I_E(\mathbf{x}) = \sum_t \left[\rho\dot{\mathbf{U}}_s\cdot\dot{\mathbf{U}}_r - \left(\underline{\underline{\mathbf{c}}}\nabla\mathbf{U}_s\right) : \nabla\mathbf{U}_r\right] , \tag{3}$$

where $\rho(\mathbf{x})$ is the density of the medium and $\underline{\underline{\mathbf{c}}}$ is the second-order stiffness tensor. The superscript dot applied on the wavefields indicates time differentiation and ∇ is the spatial gradient. The symbol : indicates Frobenius product between two matrices resulting in a scalar quantity (Golub and Loan, 1996). A more compact form of equation 3 utilizes the so-called energy vectors, which are defined as

$$\square\mathbf{U}_s = \left\{\rho^{1/2}\dot{\mathbf{U}}_s, \quad \underline{\underline{\mathbf{c}}}^{1/2}(\nabla\mathbf{U}_s)\right\} \ , \tag{4}$$

$$\square\mathbf{U}_r = \left\{\rho^{1/2}\dot{\mathbf{U}}_r, -\underline{\underline{\mathbf{c}}}^{1/2}(\nabla\mathbf{U}_r)\right\} \ . \tag{5}$$

Analyzing the terms in equations 4 and 5, one can note that the energy vectors contain twelve components, three from the terms $\rho^{1/2}\dot{\mathbf{U}}_{s,r}$ and nine from $\underline{\underline{\mathbf{c}}}^{1/2}(\nabla\mathbf{U}_{s,r})$. We can also define $\square$ as the energy operator containing derivatives and medium parameters applicable to a multicomponent wavefield. Using the definition of energy vectors, the imaging condition in equation 3 becomes

$$I_E = \sum_t \square\mathbf{U}_s\cdot\square\mathbf{U}_r \ . \tag{6}$$

In order to obtain the adjoint operator associated with the imaging condition in equation 6, we rewrite the expression in operator form:

$$\mathbf{m} = \left(\square\mathbf{U}_s\right)^{\mathrm{T}}\square\mathbf{U}_r \ . \tag{7}$$

We can write the elastic wavefields $\mathbf{U}_s$ and $\mathbf{U}_r$ in terms of a sequence of operators applied to the source function $\mathbf{d}_s$ and to the receiver data $\mathbf{d}_r$, respectively. Firstly, we implement injection of the multicomponent source function and receiver data

into the Earth model by operators $\mathbf{K}_s$ and $\mathbf{K}_r$, respectively. Secondly, we apply forward and backward elastic wavefield extrapolation operators $\mathbf{E}_+$ and $\mathbf{E}_-$. Hence, we express the wavefields by $\mathbf{U}_s = \mathbf{E}_+\mathbf{K}_s\mathbf{d}_s$ and $\mathbf{U}_r = \mathbf{E}_-\mathbf{K}_r\mathbf{d}_r$, and we can rewrite equation 7 as

$$\mathbf{m} = \left(\square\mathbf{E}_+\mathbf{K}_s\mathbf{d}_s\right)^{\mathrm{T}}\square\mathbf{E}_-\mathbf{K}_r\mathbf{d}_r \ . \tag{8}$$

Equation 8 is in the form $\mathbf{m} = \mathbf{L}^{\mathrm{T}}\mathbf{d}_r$, where

$$\mathbf{L}^{\mathrm{T}} = \left(\square\mathbf{E}_+\mathbf{K}_s\mathbf{d}_s\right)^{\mathrm{T}}\square\mathbf{E}_-\mathbf{K}_r = \left(\square\mathbf{U}_s\right)^{\mathrm{T}}\square\mathbf{E}_-\mathbf{K}_r \ . \tag{9}$$

Therefore, this chain of operators $\mathbf{L}^{\mathrm{T}}$ represents the migration based on the energy norm. We can obtain the operator $\mathbf{L}$ (adjoint of $\mathbf{L}^{\mathrm{T}}$) if we apply the adjoint for each individual operator and reverse the order of operators:

$$\mathbf{L} = \mathbf{K}_r^{\mathrm{T}}\mathbf{E}_+\square^{\mathrm{T}}\left(\square\mathbf{E}_+\mathbf{K}_s\mathbf{d}_s\right) = \mathbf{K}_r^{\mathrm{T}}\mathbf{E}_+\square^{\mathrm{T}}\square\mathbf{U}_s \ , \tag{10}$$

where $\mathbf{E}_-^{\mathrm{T}} = \mathbf{E}_+$. This chain of operators $\mathbf{L}$ represents the linearized modeling based on the energy norm, involving extraction of multicomponent single-scattered data at the receiver locations ($\mathbf{K}_r^{\mathrm{T}}$), and elastic wavefield extrapolation ($\mathbf{E}_+$) from virtual multicomponent sources computed by $\square^{\mathrm{T}}\square\mathbf{U}_s\mathbf{m}$.

To elucidate the linearized modeling based on the energy norm, here are the steps involved in computing the scattered data at receivers ($\mathbf{d}_r$):

(i) Inject the source wavelet $\mathbf{d}_s$ by utilizing $\mathbf{K}_s$.
(ii) Extrapolate ($\mathbf{E}_+$) the injected source $\mathbf{K}_s\mathbf{d}_s$, generating the background wavefield $\mathbf{U}_s$;
(iii) Compute $\square\mathbf{U}_s$, a twelve-component vector field shown in equation 4;
(iv) Multiply each component of $\square\mathbf{U}_s$ by the scalar reflectivity model $\mathbf{m}$;
(v) Compute $\square^{\mathrm{T}}\square\mathbf{U}_s\mathbf{m}$, a three-component virtual source field;
(vi) Extrapolate ($\mathbf{E}_+$) the virtual source $\square^{\mathrm{T}}\square\mathbf{U}_s\mathbf{m}$, generating the scattered wavefield $\mathbf{U}_r$;
(vii) Extract data at receiver locations $\mathbf{d}_r$ by applying $\mathbf{K}_r^{\mathrm{T}}$ to the scattered wavefield.

In Appendix A, we represent all individual operators involved in $\mathbf{L}$ and $\mathbf{L}^{\mathrm{T}}$ pictorially in order to illustrate the series of increases and reductions in dimensionality throughout our linearized modeling and migration. Also, in Appendix B, we show all the components of the virtual source term $\square^{\mathrm{T}}\square\mathbf{U}_s\mathbf{m}$ explicitly for a 2D vertical transversely isotropic (VTI) medium.

2.2 Energy-norm elastic least-squares migration

The linearized modeling operator $\mathbf{L}$ and its adjoint enables us to compute an image that minimizes the objective function

$$E\left(\mathbf{m}\right) = \frac{1}{2}\|\mathbf{L}\mathbf{m} - \mathbf{d}_r\|^2 \ . \tag{11}$$

The reflectivity that minimizes equation 11 is mathematically described as

$$\mathbf{m}^{LS} = \left(\mathbf{L}^{\mathrm{T}}\mathbf{L}\right)^{-1}\mathbf{L}^{\mathrm{T}}\mathbf{d}_r \ . \tag{12}$$

The gradient of the objective function in equation 11 with respect to a model at a given iteration i is

$$\mathbf{g}_i = \frac{\partial E\left(\mathbf{d}, \mathbf{m}_i\right)}{\partial \mathbf{m}_i} = \mathbf{L}^{\mathrm{T}}\left(\mathbf{L}\mathbf{m}_i - \mathbf{d}_r\right) \ . \tag{13}$$

The model update at each iteration can be a scaled version of the gradient, or ideally can incorporate an approximation of the Hessian operator $\mathbf{H} = \left(\mathbf{L}^{\mathrm{T}}\mathbf{L}\right)$ (Aoki and Schuster, 2009; Tang, 2009; Dai et al., 2010):

$$\mathbf{m}_{i+1} = \mathbf{m}_i - \mathbf{H}^{-1}\mathbf{g}_i \ , \tag{14}$$

For all numerical experiments shown in this paper, we set the initial model to be zero and apply an illumination compensation on the gradient at every iteration. This illumination compensation computed from the wavefields is considered to be an approximation of the Hessian operator (Rickett, 2003; Plessix and Mulder, 2004; Du et al., 2012). We use the energy norm of the source wavefield at every spatial location as our illumination compensation factor:

$$\mathbf{h}_i\left(\mathbf{x}\right) = \|\mathbf{U}_s\|_E^2 = \square\mathbf{U}_s \cdot \square\mathbf{U}_s \ , \tag{15}$$

3 EXAMPLES

The following numerical examples demonstrate how the linearized modeling and migration operators based on the energy norm behave during LSRTM. Firstly, we perform an experiment with a single flat reflector to convey some intuition about how the method works; secondly, we show an experiment using a realistic synthetic Earth model containing many reflectors and structures to test the method in more complex geological settings with sharp interfaces that create backscattering artifacts in conventional imaging methods; finally, we validate the method by applying it to a North Sea field dataset.

3.1 Single-reflector model

We demonstrate energy-based LSRTM using a model defined by vertical transversely isotropy (VTI) with a reflector at $z = 0.55$km. The model parameters are $\rho = 2.5$kg/cm^3, $V_{P0} = 2.2$km/s (P-wave velocity along the symmetry axis), $V_{S0} = 1.3$km/s (S-wave velocity along the symmetry axis), and Thomsen parameters $\epsilon = 0.4$ and $\delta = 0.3$ (Thomsen, 1986). The reflector consists of the following contrasts: $\Delta\rho = 0.7$kg/cm^3, $\Delta V_{P0} = 0.6$km/s, and $\Delta V_{S0} = 0.5$km/s. Figure 1(a) shows the density model and the acquisition geometry that consists of 10 sources and a line of receivers at the surface. We create a scalar reflectivity based on the contrast of the Earth model (Figure 1(b)). We generate shot records by two different methods: (a) full-wavefield modeling, which uses the Earth model with contrasts as conventionally implemented to generate synthetic elastic data; (b) linearized modeling based on the energy norm, which applies the operator in equation 10 to the reflectivity from Figure 1(b) using the background Earth model (without contrast). We migrate both synthetic datasets using the energy imaging condition from

equation 3. Figures 1(c) and 1(d) show the stacked RTM images that use the full-modeled data and linearized-modeled data, respectively. We also compute 10 iterations of LSRTM for both datasets: Figures 1(e) and 1(e) show the final stacked LSRTM images that use the full-modeled data and linearized modeled data, respectively. By comparing the LSRTM images with their RTM counterparts, one can observe the better quality of LSRTM images: the artifacts caused by the truncated acquisition are attenuated and the amplitudes are closer to the true reflectivity.

One can note that the RTM and LSRTM images using the linearized modeled data have less artifacts than the ones using the full-modeled data. To explain why, we show both synthetic datasets in Figures 2(a) and 2(b). From early to late arrival times, the three visible events in each dataset correspond to (1) P-P (apex around $t = 0.6$s), (2) P-S/S-P (apex around $t = 0.8$s), and (3) S-S reflections (apex around $t = 0.9$s). For the near offsets, we notice that events in both datasets match in phase and polarity because only specular reflections exist at these near offsets. However, since the linearized modeling is a simplification of full-wavefield modeling, it can only predict single-scattering events and cannot predict wave phenomena that are beyond the critical angle, such as head waves, and these phenomena influence the amplitude of the three events at the far offsets of Figure 2(a). One can also notice such behavior on the data residuals at iteration 10 (Figures 2(c) and 2(d)). The linearized modeling embedded in the engine of both LSRTM results can only predict amplitude from reflections events, and cannot match the far-offset amplitudes from the full-modeled data (Figure 2(c)). Alternatively, by using the same linearized modeling operator to generate synthetic data, the data residual (Figure 2(d)) and its related objective function (Figure 2(e)) decrease substantially more and are close to zero at the last iteration, as our operators are proper adjoints of each other, and can perfectly match the dataset containing only reflections after several iterations.

3.2 2007 BP TTI anisotropic benchmark model

We use a portion of the 2007 BP tilted transversely isotropic (TTI) benchmark model to test the method in a more complicated synthetic model. The original model consists of V_{P0}, ϵ, δ, and the tilt of the symmetry axis at every point (ν); we create V_{S0} and ρ from V_{P0} (Figure 3). The experiment geometry consists of 55 pressure sources equally spaced in the water at the surface ($z = 0.092$km), and a line of multicomponent receivers at every grid point at the water bottom, which varies between the depths of $z = 1.0$km and $z = 1.4$km. Similarly to the preceding example, we generate two different datasets by (a) full-wavefield modeling, using the density model with contrasts (Figure 3(f)), and (b) linearized modeling, using a constant density model and the reflectivity model in Figure 4(e) to generate reflections. All other Earth model parameters are kept the same between the two experiments.

We obtain energy RTM and LSRTM images using linearized-modeled data (Figures 4(a) and 4(c)) and full-modeled data (Figures 4(b) and 4(d)). We apply a power gain with depth on the RTM images for a fair comparison with LSRTM images, since RTM images commonly have weaker amplitudes for greater depths and these amplitudes can easily be compensated by such gain. Notice that artifacts in the shallow part (mainly caused by the limited acquisition) are attenuated, and the deep reflectors as well as the salt flanks are better illuminated in the LSRTM images compared to their RTM counterparts. Both LSRTM images contain sharper reflectors and are closer to the assumed true reflectivity models shown in Figures 4(e) and 4(f). For the LSRTM images, one can observe low-wavenumber artifacts inside the salt because most of the waves in this region do not scatter towards the receivers due to this particular experiment, which images only one side of the salt body. These events create artifacts that accumulate over iterations, and they are part of the null space for the inversion, i.e., they do not predict any reflections in the observed data. Although such artifacts do not represent actual reflectors, they are not harmful to the inversion process since they reside in the null space of the reflectivity model and do not mask any reflectors inside the salt body.

In Figures 5(a) and 5(b), we show the observed data at a particular shot location ($x = 41.4$km) containing offsets up to 8km for linearized and full-wavefield modeling, respectively. The corresponding data residuals after 20 iterations are shown in Figures 5(c) and 5(d), which are diminished when compared to the original datasets. The objective functions for both experiments are shown in Figure 5(e). As expected, the objective function for the inversion using the dataset generated with the linearized modeling operator itself converges to zero, as our migration and modeling operators are proper adjoints of each other. The objective function for the experiment with full-modeled data decreases substantially and can potentially decrease more if more iterations are allowed, since the objective function at iteration 20 retains a significant slope, as seen in Figure 5(e). However, we expect the rate of convergence to be smaller over iterations until the objective function reaches a plateau, because our modeling operator cannot predict events beyond single-scattering in full-modeled data. In addition, differently from the single-reflector preceding example, several reflectors in this Earth model cause multiple scattering events during full-wavefield modeling that are also not predicted by our linearized modeling operator. All events that exist in the data and are not predicted by our operator might form artifacts in the image, as for any other migration methods applied on data that contains multiple reflections, turning waves, etc.

3.3 Volve OBC real dataset

We apply the method to a field dataset acquired by an ocean-bottom cable (OBC) in the Volve field, located in the North Sea (Szydlik et al., 2007). Although the original dataset is 3D, we use a 2D section near the central crossline to reduce computational cost. The Earth model is elastic VTI and the corresponding parameters are shown in Figure 6. The prominent layer around $z = 3$ km is a chalk layer that corresponds to the hydrocarbon reservoir. The dataset provided was pre-processed to retain only the down-going pressure component, and a par-

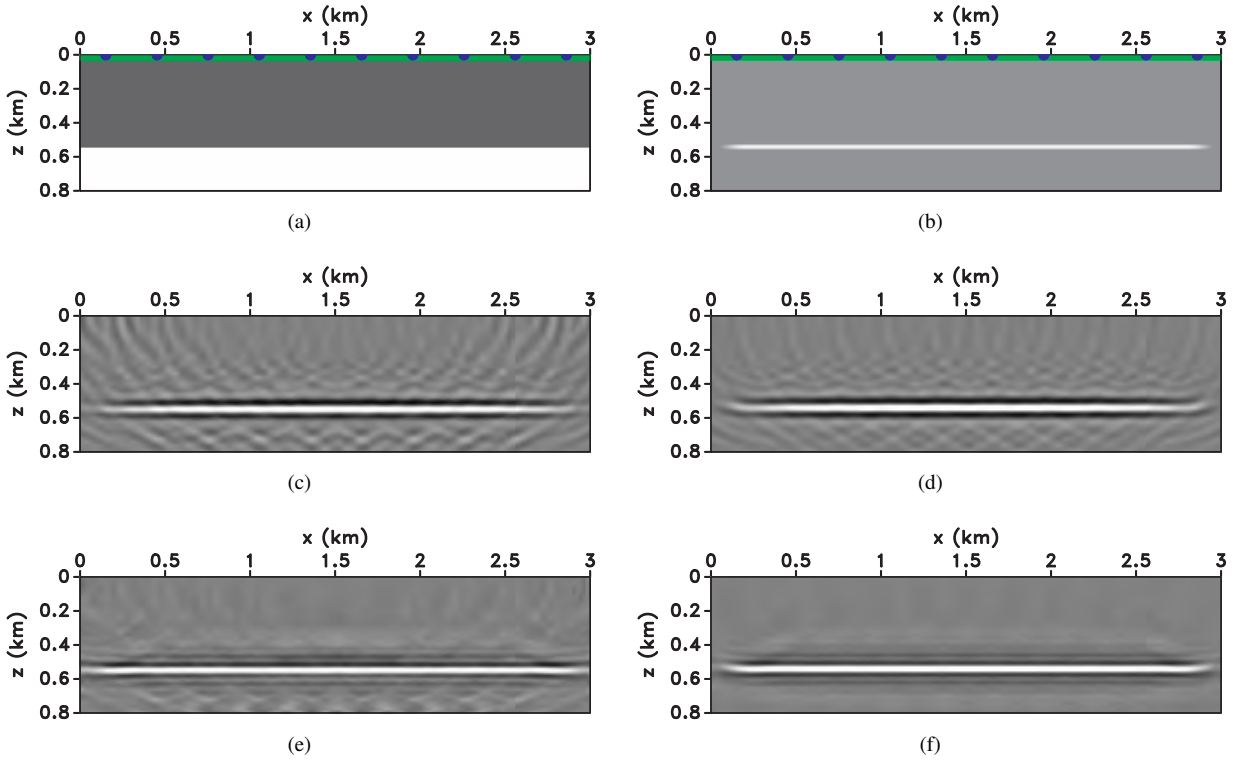

Figure 1. (a) Density model used in full-wavefield modeling, and (b) reflectivity model used in linearized modeling. The acquisition geometry consists of 10 sources (blue) and a line of receivers (green). Elastic energy RTM image with (c) full-modeled data and with (d) linearized-modeled data. Elastic energy LSRTM image with (e) full-modeled data and with (f) linearized-modeled data. Note how LSRTM attenuates artifacts caused by sparse acquisition.

ticular common shot gather for a source at $x = 6.3$km is shown in Figure 7(a). We obtain energy RTM and LSRTM images after 15 iterations, shown in Figures 8(a) and Figure 8(b), and the corresponding objective function in Figure 7(d). The LSRTM image exhibits more detailed reflectors compared to the RTM image, and enhances the amplitudes at the edges of the model. With a smooth muting of far-offset events, the objective function decreases substantially reaching 40% of its initial value at the last iteration. By comparing the modeled data and residual at the last iteration (Figures 7(c) and 7(b)), and the observed data (Figure 7(a)), one can note that our linearized modeling operator and the image at the last iteration predict the main reflections and do not predict events such as noise, direct arrival, far-offset amplitudes, etc.

4 CONCLUSIONS

We propose an elastic LSRTM method that uses imaging operators based on the energy norm and delivers a scalar image that contains attenuated artifacts and explains data at receiver locations. The absence of strong backscattering artifacts in our results shows the advantage of our migration operator compared to its conventional counterparts. Using displacement fields directly and without costly wave-mode decomposition, our linearized modeling operator generates multicomponent datasets with a scalar reflectivity that correctly predicts the amplitude and phase of the reflections in observed data, as illustrated by the final modeled data and objective functions from our numerical examples. As for any other linearized modeling procedure, events that are not reflections are inaccurately predicted by our linearized operator, and these events show in the image as artifacts. Future work involves application of our method to another multicomponent field dataset that contains both vertical and horizontal displacement components, and to 3D Earth models.

5 ACKNOWLEDGMENTS

We thank the sponsors of the Center for Wave Phenomena, whose support made this research possible. We acknowledge Hemang Shah and BP Exploration Operation Company Limited for creating the TTI model. We are grateful to Statoil ASA and the Volve license partners ExxonMobil E&P Norway AS and Bayerngas Norge AS for the release of the Volve data. We would like to thank Marianne Houbiers at Statoil for helping us with the Volve dataset. We acknowledge Antoine Guitton for helpful discussions. The synthetic examples in this pa-

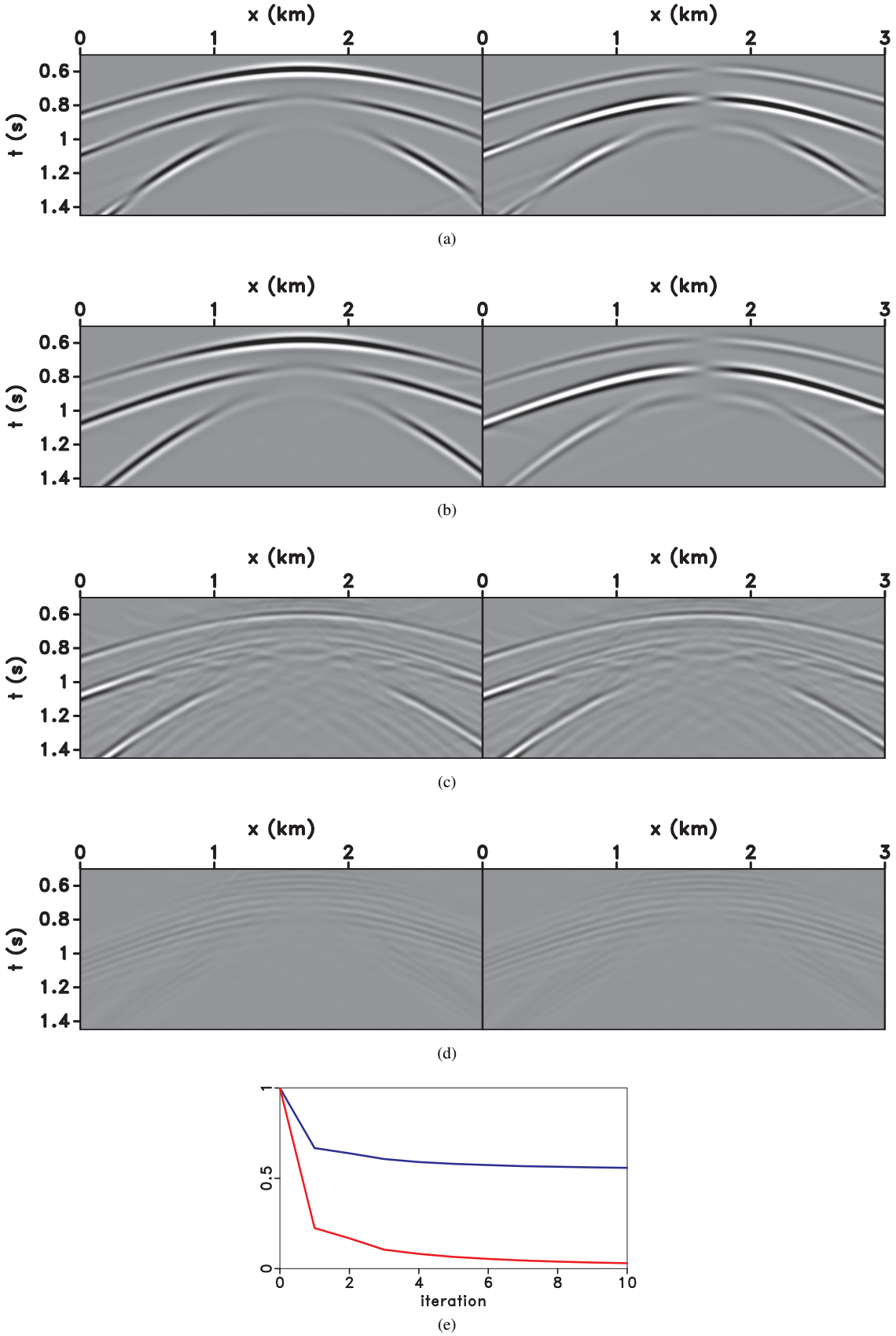

Figure 2. Vertical- (left) and horizontal- (right) component data from (a) full modeling and from (b) linearized modeling. Data residuals from the LSRTM images using (c) full modeling and from (d) linearized modeling. (e) Normalized objective functions for inversion using full-modeled data (blue) and linearized data (red). The far-offset amplitudes from full-modeled data are not correctly predicted by the linearized modeling operator.

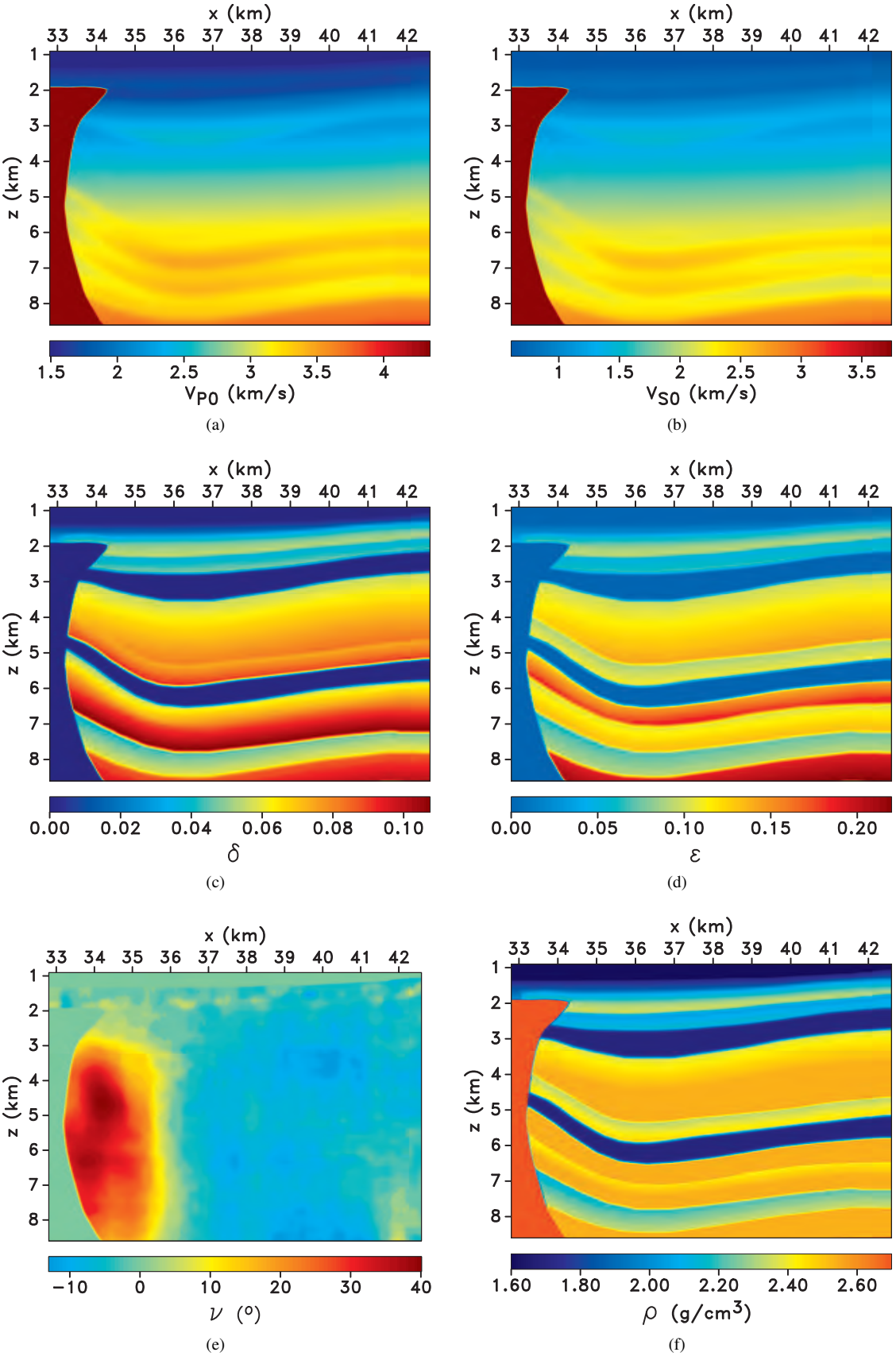

Figure 3. BP TTI model parameters: (a) P-wave and (b) S-wave velocities along the symmetry axis; Thomsen parameters (c) δ and (d) ϵ along the symmetry axis; (e) tilt of the symmetry axis (ν); (f) density with contrasts for full-wavefield modeling experiment.

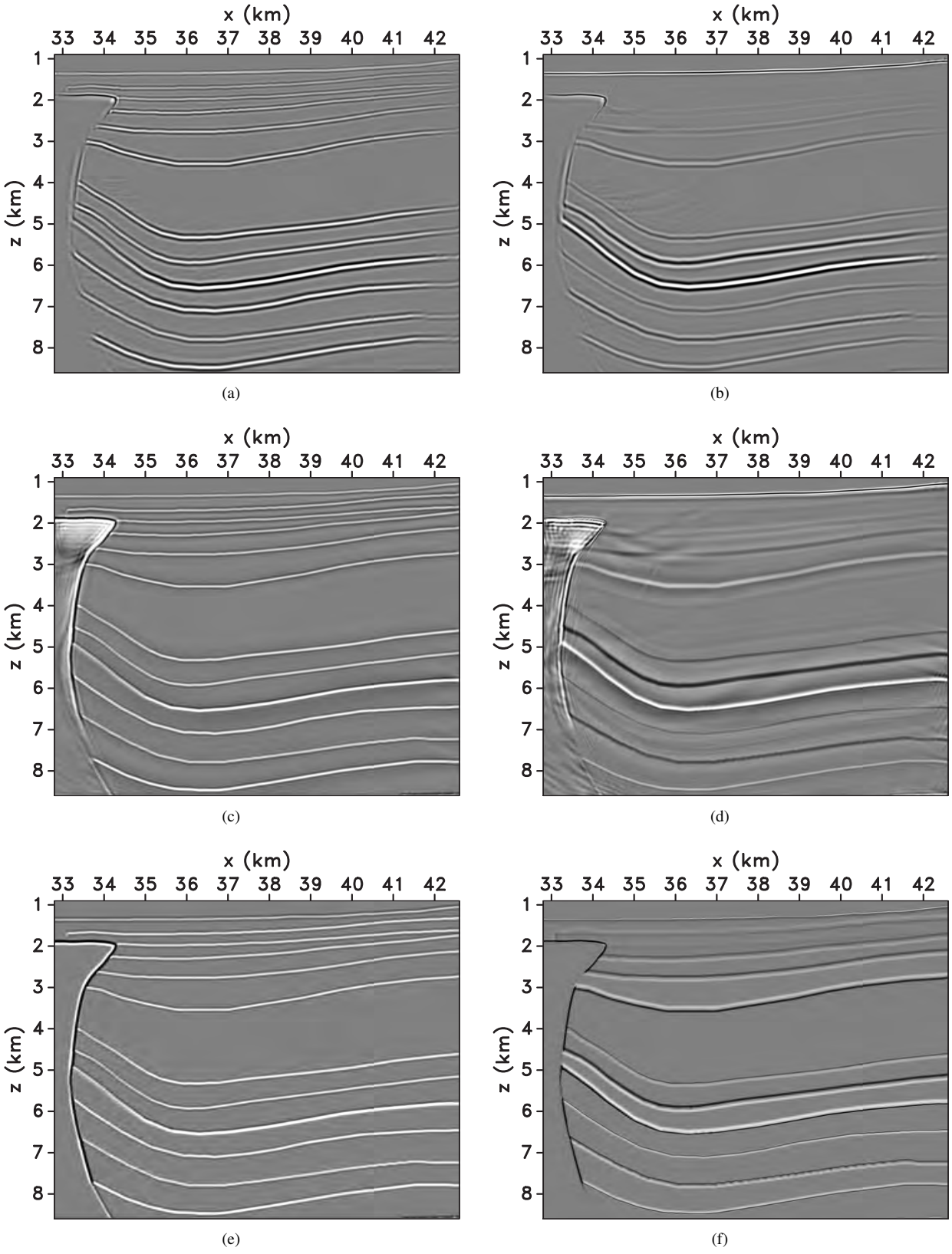

Figure 4. RTM images using (a) linearized-modeled data and (b) full-modeled data. LSRTM images after 20 iterations using (c) linearized-modeled data and (d) full-modeled data. (e) True reflectivity model for linearized-modeled data and (f) Laplacian operator applied on the density model in Figure 3(f) in order to show contrasts that create reflections in the full-wavefield modeling.

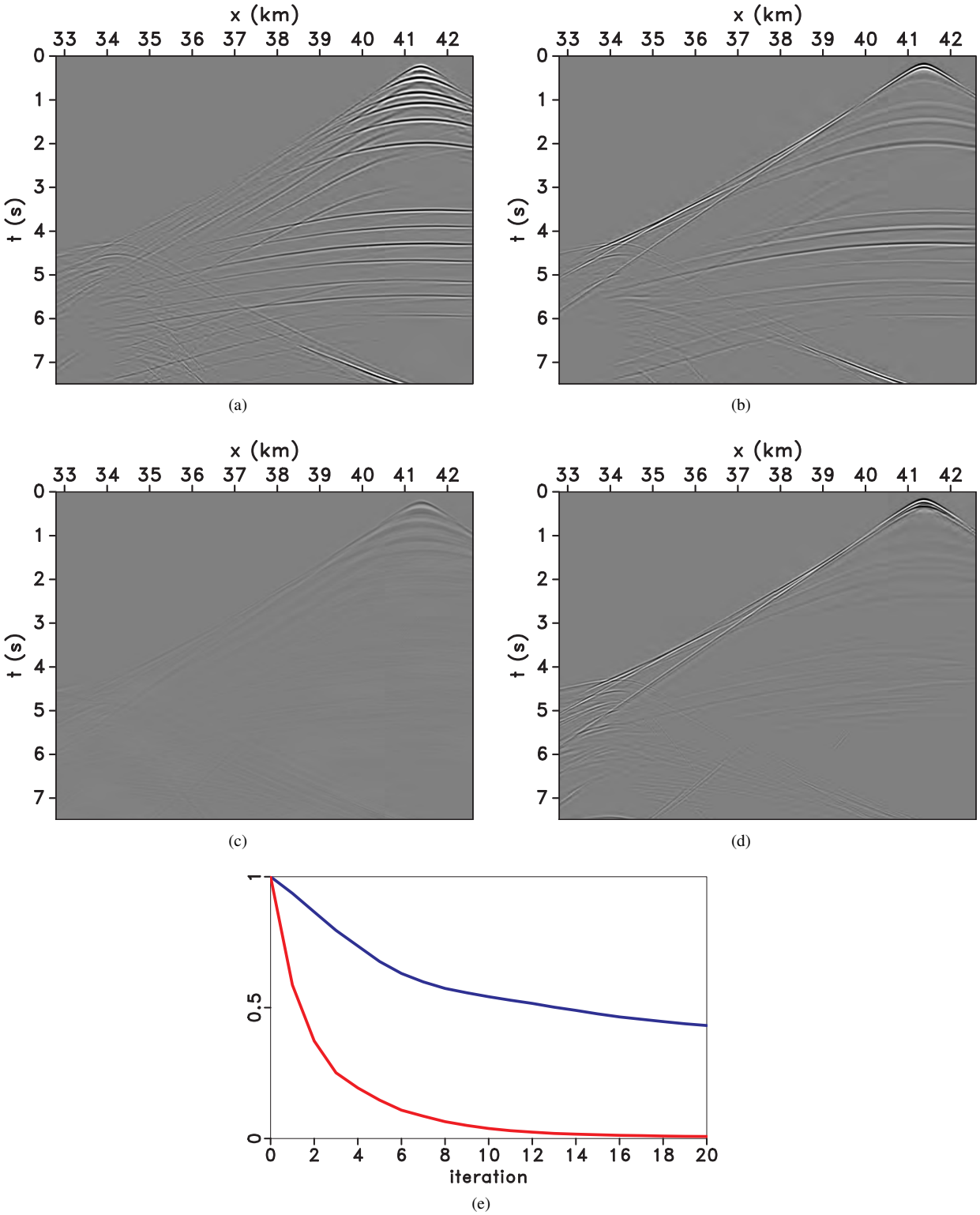

Figure 5. Vertical component of observed data at a $x_s = 41.4$km obtained by (a) linearized modeling using the reflectivity model in Figure 4(e), and (b) full-wavefield modeling using density model in Figure 3(f). Vertical component data residuals after 20 iterations for (c) linearized and (d) full-wavefield modeling experiments. (e) Normalized objective function for experiments using (red) linearized and (blue) full-modeled data.

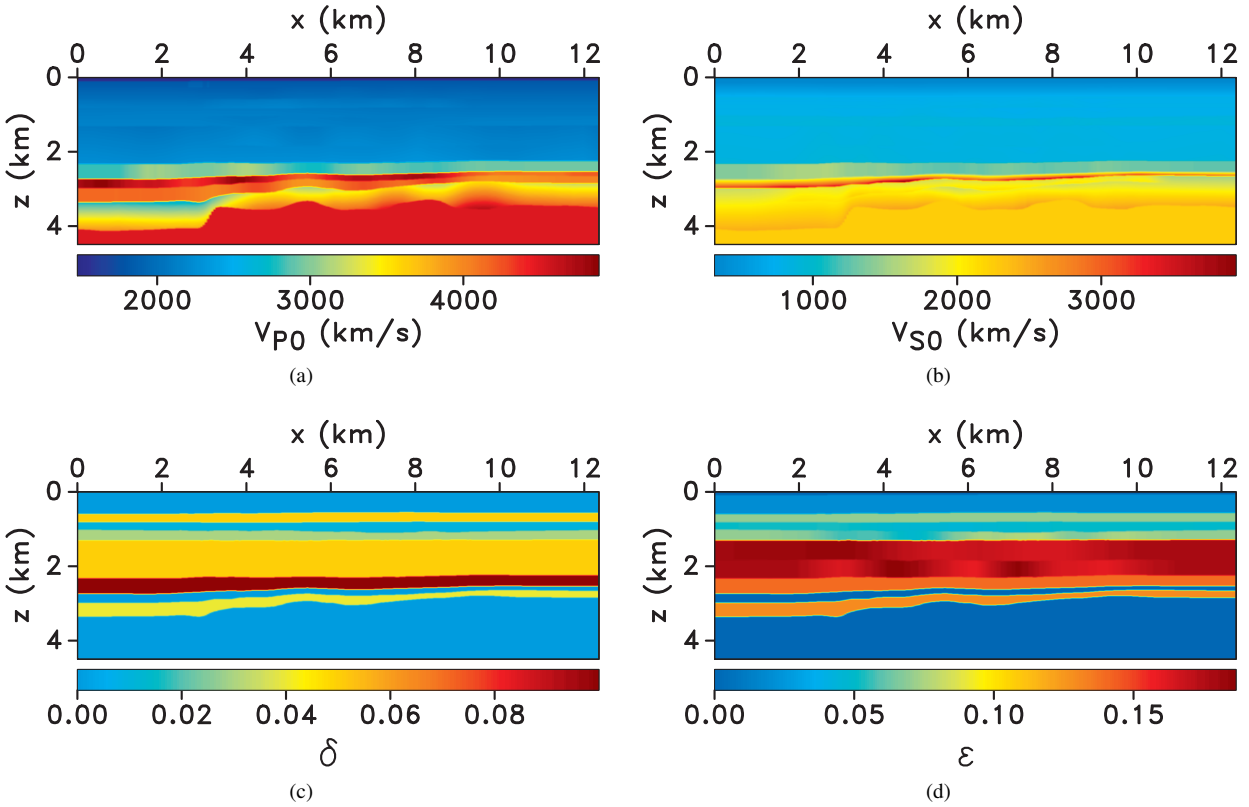

Figure 6. Volve 2D model parameters: (a) P-wave and (b) S-wave velocities along the vertical symmetry axis; Thomsen parameters (c) δ and (d) ϵ.

per use the Madagascar open-source software package (Fomel et al., 2013) freely available from http://www.ahay.org.

REFERENCES

Alves, G., and B. Biondi, 2016, Imaging condition for elastic reverse time migration: 86th Annual International Meeting, SEG, Expanded Abstracts, 3959–3965.

Aoki, N., and G. T. Schuster, 2009, Fast least-squares migration with a deblurring filter: Geophysics, **74**, no. 6, WCA83–WCA93.

Baysal, E., D. D. Kosloff, and J. W. C. Sherwood, 1983, Reverse time migration: Geophysics, **48**, 1514–1524.

Chang, W.-F., and G. A. McMechan, 1987, Elastic reverse-time migration: Geophysics, **52**, 1365–1375.

Chavent, G., and R.-E. Plessix, 1999, An optimal true–amplitude least–squares prestack depth–migration operator: Geophysics, **64**, 508–515.

Cheng, J., and S. Fomel, 2014, Fast algorithms for elastic-wave-mode separation and vector decomposition using low-rank approximation for anisotropic media: Geophysics, **79**, no. 4, C97–C110.

Claerbout, J. F., 1992, Earth soundings analysis: Processing versus inversion: Blackwell Scientific Publications.

Dai, W., C. Boonyasiriwat, and G. Schuster, 2010, 3D multisource least-squares reverse-time migration: 80th Annual International Meeting, SEG, Expanded Abstracts, 3120–3124.

Dong, S., J. Cai, M. Guo, S. Suh, Z. Zhang, B. Wang, and Z. Li, 2012, Least-squares reverse time migration: towards true amplitude imaging and improving the resolution: 82rd Annual International Meeting, SEG, Expanded Abstracts.

Du, Q., M. Zhang, G. Fang, X. Gong, and C. Guo, 2014, Relatively amplitude-preserved ADCIGs based on elastic RTM by modifying the initial condition as the boundary condition: 84th Annual International Meeting, SEG, Expanded Abstracts, 1888–1893.

Du, X., R. Fletcher, E. Mobley, and E. Yarman, 2012, Source and Receiver Illumination Compensation for Reverse-time Migration: 74th European Association of Geoscientists and Engineers Conference and Exhibition.

Duan, Y., P. Sava, and A. Guitton, 2016, Elastic least-squares reverse time migration: 86th Annual International Meeting, SEG, Expanded Abstracts, 3959–3965.

Dutta, G., and G. T. Schuster, 2014, Attenuation compensation for least-squares reverse time migration using the viscoacoustic-wave equation: Geophysics, **79**, no. 6, S251–S262.

Farmer, P., Z. Z. Zhou, and D. Jones, 2009, The role of reverse time migration in imaging and model estimation: The Leading Edge, **28**, no. 4, 436–441.

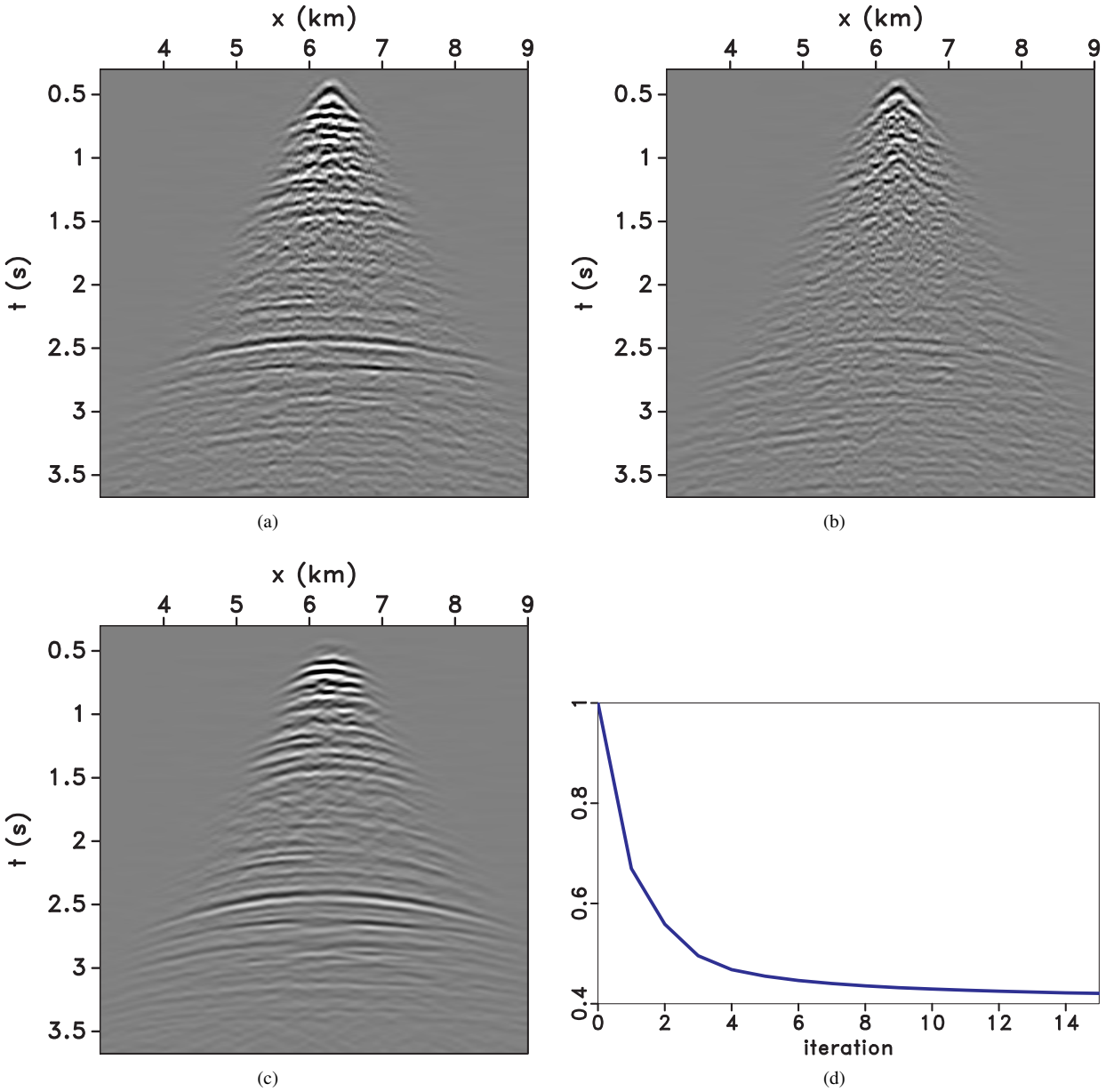

Figure 7. Volve experiment: (a) observed, (b) residual and (c) modeled (after 15 iterations) pressure shot gathers for a source at $x = 6.4$km. The main reflections are correctly predicted by our modeling operator. (c) Normalized objective function for LSRTM.

Feng, Z., and G. T. Schuster, 2016, Elastic least-squares reverse time migration: 86th Annual International Meeting, SEG, Expanded Abstracts, 3959–3965.

Fomel, S., P. Sava, I. Vlad, Y. Liu, and V. Bashkardin, 2013, Madagascar: open-source software project for multidimensional data analysis and reproducible computational experiments: Journal of Open Research Software, 1:e8, DOI: http://dx.doi.org/10.5334/jors.ag.

Golub, G. H., and C. F. V. Loan, 1996, *in* Matrix computations, 3rd ed.: John Hopkins University Press.

Hobro, J. W. D., C. H. Chapman, and J. O. A. Robertsson, 2014, A method for correcting acoustic finite-difference amplitudes for elastic effects: Geophysics, **79**, no. 4, T243–T255.

Hokstad, K., R. Mittet, and M. Landrø, 1998, Elastic reverse time migration of marine walkaway vertical seismic profiling data: Geophysics, **63**, 1685–1695.

Huang, J., D. Si, Z. Li, and J. Huang, 2016, Plane-wave least-squares reverse time migration in complex VTI media: 86th Annual International Meeting, SEG, Expanded Abstracts,

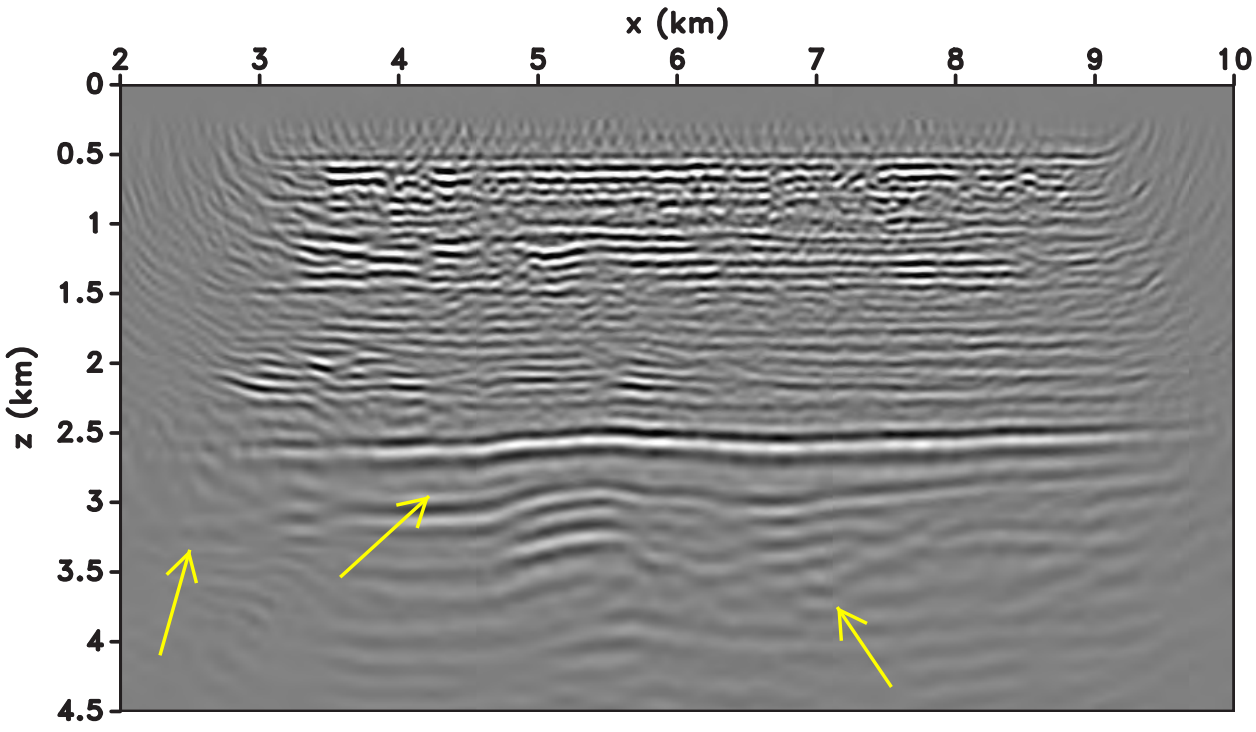

(a)

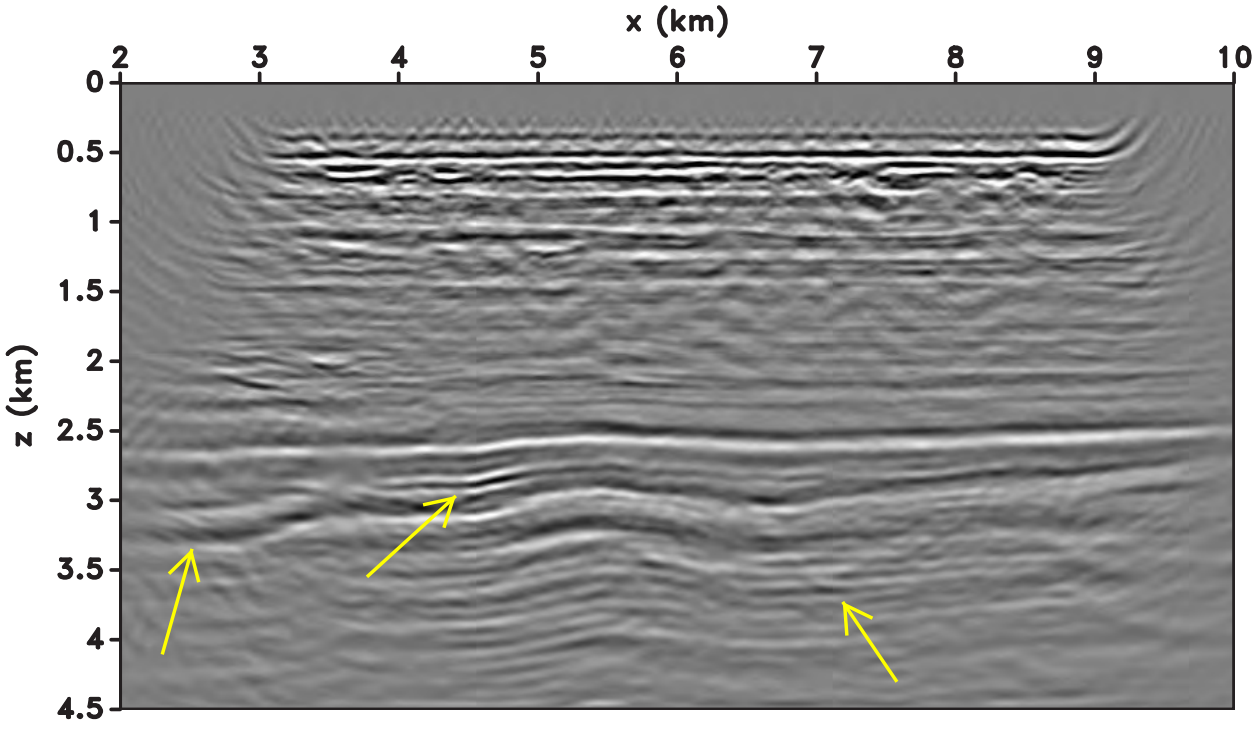

(b)

Figure 8. Volve experiment: energy (a) RTM and (b) LSRTM images. Reflectors around $z = 3.0$km become sharper, especially at the edges of the image. The arrows indicate reflectors that become more visible in the LSRTM image relative to RTM.

441–446.
Kuhl, H., and M. D. Sacchi, 2003, Least-squares wave-equation migration for AVO/AVA inversion: Geophysics, **68**, 262–273.
Lailly, P., 1983, The seismic inverse problem as a sequence of before stack migrations: Conference on Inverse Scattering, Theory and Application: Society of Industrial and Applied Mathematics, Expanded Abstracts, 206–220.
Levin, S. A., 1984, Principle of reverse-time migration: Geophysics, **49**, 581–583.
Lu, R., P. Traynin, and J. E. Anderson, 2009, Comparison of elastic and acoustic reverse–time migration on the synthetic elastic Marmousi–II OBC dataset: 79th Annual International Meeting, SEG, Expanded Abstracts, 2799–2803.
McMechan, G. A., 1983, Migration by extrapolation of time dependent boundary values: Geophysical Prospecting, **31**, 413–420.
Nemeth, T., C. Wu, and G. T. Schuster, 1999, Least–squares migration of incomplete reflection data: Geophysics, **64**, 208–221.
Phadke, S., and S. Dhubia, 2012, Reverse time migration of marine models with elastic wave equation and amplitude preservation: 82nd Annual International Meeting, SEG, Expanded Abstracts.
Plessix, R., and W. Mulder, 2004, Frequency-domain finite-difference amplitude-preserving migration: Geophysical Journal International, **157**, 975–987.
Ren, Z., Y. Liu, and M. K. Sen, 2017, Least-squares reverse time migration in elastic media: Geophysical Journal International, **208**, no. 2, 1103–1125.
Rickett, J. E., 2003, Illumination-based normalization for wave-equation depth migration: Geophysics, **68**, 1371–1379.
Rocha, D., N. Tanushev, and P. Sava, 2017, Anisotropic elastic wavefield imaging using the energy norm: Geophysics, **82**, no. 3, S225–S234.
Sripanich, Y., S. Fomel, J. Sun, and J. Cheng, 2015, Elastic wave-vector decomposition in orthorhombic media: 85th Annual International Meeting, SEG, Expanded Abstracts, 498–503.
Sun, J., S. Fomel, and T. Zhu, 2015, Preconditioning least-squares RTM in viscoacoustic media by Q-compensated RTM: 85th Annual International Meeting, SEG, Expanded Abstracts, 3959–3965.
Szydlik, T., P. Smith, S. Way, L. Aamodt, and C. Friedrich, 2007, 3D PP/PS prestack depth migration on the Volve field: First Break, **25**, no. 4, 4347.
Tang, Y., 2009, Target-oriented wave-equation least-squares migration/inversion with phase–encoded hessian: Geophysics, **74**, no. 6, WCA95–WCA107.
Thomsen, L., 1986, Weak elastic anisotropy: Geophysics, **51**, 1954–1966.
Wang, W., G. A. McMechan, C. Tang, and F. Xie, 2016, Up/down and P/S decompositions of elastic wavefields using complex seismic traces with applications to calculating Poynting vectors and angle-domain common-image gathers from reverse time migrations: Geophysics, **81**, no. 4, S181–S194.
Xu, L., A. Stanton, and M. D. Sacchi, 2016, Elastic least squares reverse time migration: 86th Annual International Meeting, SEG, Expanded Abstracts, 3959–3965.
Yan, J., and P. Sava, 2007, Elastic wavefield imaging with scalar and vector potentials: 77th Annual International Meeting, SEG, Expanded Abstracts, 2150–2154.
———, 2009, Elastic wave-mode separation for VTI media: Geophysics, **74**, WB19–WB32.
———, 2011, Elastic wave-mode separation for tilted transverse isotropy media: Geophysical Prospecting, **60**, 29–48.
Yao, G., and H. Jakubowicz, 2012, Least-Squares Reverse-Time Migration: 82rd Annual International Meeting, SEG, Expanded Abstracts.
Zhang, Q., and G. A. McMechan, 2010, 2D and 3D elastic wavefield vector decomposition in the wavenumber domain for VTI media: Geophysics, **75**, D13–D26.
Zhang, Y., and J. Sun, 2009, Practical issues in reverse time migration: true amplitude gathers, noise removal and harmonic source enconding: First Break, **27**, 53–59.

Appendix A

Energy-based modeling and migration operators

The energy image $\mathbf{m}\,(\mathbf{x})$ is obtained by the expression

$$\mathbf{m} = (\square \mathbf{U}_s)^{\mathrm{T}}\, \square \mathbf{U}_r \ , \tag{A.1}$$

which can be represented schematically as

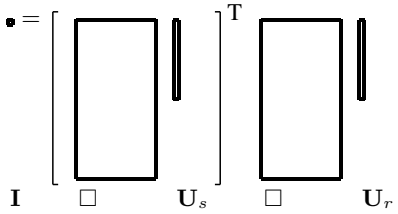

The operator $\square$ turns a three-component displacement field into a twelve-component vector field that contains spatial and temporal derivatives. Equation A.1 also implies summation over time. We represent this increase in dimensions pictorially by making the matrix of $\square$ considerably larger than the wavefield vectors $\mathbf{U}_s$ and $\mathbf{U}_r$. Using extrapolator and injection operators, as explained in the body of the paper, we have

$$\mathbf{m} = (\square \mathbf{E}_+ \mathbf{K}_s \mathbf{d}_s)^{\mathrm{T}}\, \square \mathbf{E}_- \mathbf{K}_r \mathbf{d}_r \ . \tag{A.2}$$

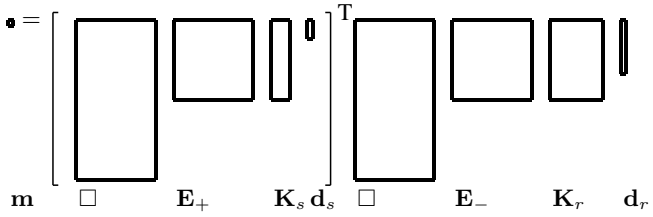

In compact form, we can rewrite equation A.2 as

$$\mathbf{m} = \mathbf{L}^{\mathrm{T}} \mathbf{d}_r \ . \tag{A.3}$$

Linearized modeling is defined as

$$\mathbf{d}_r = \mathbf{L}\mathbf{m}\ . \tag{A.4}$$

Based on equation A.2, we can rewrite equation A.4 as

$$\mathbf{d}_r = \mathbf{K}_r^{\mathrm{T}}\mathbf{E}_-^{\mathrm{T}}\square^{\mathrm{T}}\square\mathbf{U}_s\mathbf{m}\ , \tag{A.5}$$

which is represented schematically as

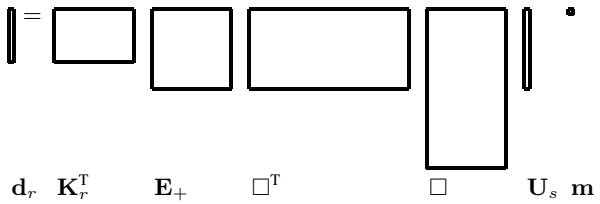

or

$$\mathbf{d}_r = \mathbf{K}_r^{\mathrm{T}}\mathbf{E}_+\square^{\mathrm{T}}\square\left(\mathbf{E}_+\mathbf{K}_s\mathbf{d}_s\right)\mathbf{m}\ . \tag{A.6}$$

represented as

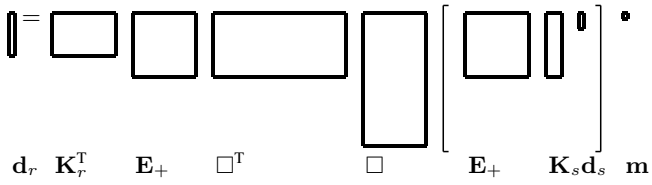

The virtual multicomponent source computed for the generation of the scattered wavefield is represented by the chain of operators $\square^{\mathrm{T}}\square\left(\mathbf{E}_+\mathbf{K}_s\mathbf{d}_s\right)\mathbf{m} = \square^{\mathrm{T}}\square\mathbf{U}_s\mathbf{m}$:

Appendix B

Multicomponent virtual source for 2D VTI modeling

We can write the energy imaging condition (equation 3) for a two-dimensional vertical transversely isotropic medium in matrix notation as

$$I_E\left(\mathbf{x}\right) = \rho\begin{bmatrix}\dot{U}_1^s & \dot{U}_3^s\end{bmatrix}\begin{bmatrix}\dot{U}_1^r\\ \dot{U}_3^r\end{bmatrix} \quad - \\ \begin{bmatrix}C_{11}U_{1,1}^s + C_{13}U_{3,3}^s & C_{55}\left(U_{1,3}^s + U_{3,1}^s\right)\\ C_{55}\left(U_{1,3}^s + U_{3,1}^s\right) & C_{33}U_{3,3}^s + C_{13}U_{1,1}^s\end{bmatrix} \quad : \\ \begin{bmatrix}U_{1,1}^r & U_{3,1}^r\\ U_{1,3}^r & U_{3,3}^r\end{bmatrix} \quad , \tag{B.1}$$

where $U_{i,j}^{s,r}$ is the j-th derivative of the ith-component of wavefield $\mathbf{U}_s$ or $\mathbf{U}_r$, and C_{ij} are the stiffness coefficients in Voigt notation. The symbol : represents Frobenius product between two matrices: an element-wise product between matrices with the corresponding sum of the products resulting in a scalar. Indices $i, j = \{1, 2, 3\}$ refer to $\{x, y, z\}$. The superscript dot on $U_i^{s,r}$ indicates time differentiation. Rewriting all derivatives applied to U^r as operators, we obtain

$$I_E = \rho\begin{bmatrix}\dot{U}_1^s & \dot{U}_3^s\end{bmatrix}\begin{bmatrix}D_t & 0\\ 0 & D_t\end{bmatrix}\begin{bmatrix}U_1^r\\ U_3^r\end{bmatrix} \quad - \\ \begin{bmatrix}C_{11}U_{1,1}^s + C_{13}U_{3,3}^s & C_{55}\left(U_{1,3}^s + U_{3,1}^s\right)\\ C_{55}\left(U_{1,3}^s + U_{3,1}^s\right) & C_{33}U_{3,3}^s + C_{13}U_{1,1}^s\end{bmatrix} \quad : \\ \begin{bmatrix}D_1 & 0\\ 0 & D_3\end{bmatrix}\begin{bmatrix}U_1^r & U_3^r\\ U_1^r & U_3^r\end{bmatrix} \quad , \tag{B.2}$$

where D_t, D_1, and D_3 indicate derivative operators in time, x, and z, respectively. Therefore, the application of the energy imaging condition can be considered as an operator acting on the receiver wavefield $[U_1^r\ U_3^r]$. Its adjoint operator (linearized modeling) acts on the image (or reflectivity) I_E:

$$[f_1\ f_3] = \left[\begin{bmatrix}D_t^{\mathrm{T}} & 0\\ 0 & D_t^{\mathrm{T}}\end{bmatrix}\begin{bmatrix}\dot{U}_1^s\\ \dot{U}_3^s\end{bmatrix}\rho I_E\right]^{\mathrm{T}} - \begin{bmatrix}D_1^{\mathrm{T}} & D_3^{\mathrm{T}}\end{bmatrix} \\ \begin{bmatrix}C_{11}U_{1,1}^s + C_{13}U_{3,3}^s & C_{55}\left(U_{1,3}^s + U_{3,1}^s\right)\\ C_{55}\left(U_{1,3}^s + U_{3,1}^s\right) & C_{33}U_{3,3}^s + C_{13}U_{1,1}^s\end{bmatrix} I_E\ , \tag{B.3}$$

where $[f_1\ f_3]$ is a two-component virtual source that generates the scattered wavefield $[U_1^r\ U_3^r]$. We can rewrite the expression for each component individually for such virtual source:

$$\begin{aligned} f_1(\mathbf{x},t) = \quad & D_t^{\mathrm{T}}\ \rho D_t U_1^s I_E - \\ & D_1^{\mathrm{T}}\ \left[C_{11}D_1U_1^s + C_{13}D_3U_3^s\right] I_E - \\ & D_3^{\mathrm{T}}\ \left[C_{55}\left(D_3U_1^s + D_1U_3^s\right)\right] I_E\ , \end{aligned} \tag{B.4}$$

$$\begin{aligned} f_3(\mathbf{x},t) = \quad & D_t^{\mathrm{T}}\ \rho D_t U_3^s I_E - \\ & D_1^{\mathrm{T}}\ \left[C_{55}\left(D_3U_1^s + D_1U_3^s\right)\right] I_E - \\ & D_3^{\mathrm{T}}\ \left[C_{33}D_3U_3^s + C_{13}D_1U_1^s\right] I_E\ . \end{aligned} \tag{B.5}$$

Therefore, we can consider the generation of the energy scattered wavefield in an elastic 2D VTI medium as the extrapolation of a virtual multicomponent source defined by equations B.4 and B.5.